Multi-shell nanocomposites based multienzyme mimetics for efficient intracellular antioxidation

Yongjian Ai[1], Jinzhi You[1], Jianyi Gao[2], Jiaping Wang[2], Hong-bin Sun[3], Mingyu Ding[1], and Qionglin Liang[1] (✉)

[1] MOE Key Laboratory of Bioorganic Phosphorus Chemistry & Chemical Biology, Beijing Key Lab of Microanalytical Methods & Instrumentation, Center for Synthetic and Systems Biology, Department of Chemistry, Tsinghua University, Beijing 100084, China
[2] China Astronaut Research and Training Center, Beijing 100094, China
[3] Department of Chemistry, Northeastern University, Shenyang 110819, China

ABSTRACT

Oxidative stress is associated with many acute and chronic inflammatory diseases. Development of nanomaterial-based enzyme mimetics for reactive oxygen species (ROS) scavenging is challenging, but holds great promise for the treatment of inflammatory diseases. Herein, we report the highly ordered manganese dioxide encapsulated selenium-melanin (Se@Me@MnO$_2$) nanozyme with high efficiency for intracellular antioxidation and anti-inflammation. The Se@Me@MnO$_2$ nanozyme is sequentially fabricated through the radical polymerization and the *in-situ* oxidation-reduction. *In vitro* experimental results demonstrated that the Se@Me@MnO$_2$ nanozyme exhibits multiple enzyme activities to scavenge ROS, including catalase (CAT), glutathione peroxidase (GPx) and superoxide dismutase (SOD). Mechanism researches illustrated that the Se core possesses GPx-like catalytic activity, the Me and the MnO$_2$ possess both the SOD-like and the CAT-like activities. What's more, due to the stable unpaired electrons existing in the nanozyme, the Se, Me and MnO$_2$ provide synergistic and fast electron transfer effect to achieve the quickly scavenging of hydrogen peroxide, hydroxyl radical, and superoxide anion. Further *in vivo* experimental results showed that this biocompatible nanozyme exhibits cytoprotective effects by resisting ROS-mediated damage, thereby alleviating the inflammation. This multienzyme mimetics is believed to be an excellent ROS scavenger and have a good potential in clinical therapy for ROS-related diseases.

KEYWORDS

oxidative stress, reactive oxygen species, multienzyme mimetics, nanozymes, intracellular antioxidation, anti-inflammation

1   Introduction

Reactive oxygen species (ROS), such as the hydrogen peroxide (H_2O_2), hydroxyl radical (HO$^\bullet$), and superoxide anion ($O_2^{\bullet-}$), can be sustainably produced through the metabolic processes [1–4]. As the essential secondary messengers, ROS plays significant role in the regulation of biological organism's physiological functions, such as cell signaling, pathogen defense, and homeostasis [5–9]. However, excessive and uncontrolled ROS can arouse oxidative stress which can give risk to irreversible damage of tissue and organ through destroying proteins, nucleic acids and lipids, and finally lead to various diseases, such as cancer, stroke and neurologic disorders [10–13]. Inflammation is closely associated with oxidative stress as the natural defensive reaction to stimuli of infections, injuries and toxins. In order to protect the organism from inflammation induced by oxidative stress, it is necessary to scavenge excess ROS to maintain intracellular redox balance [14–18]. Broad-spectrum antioxidants such as *N*-acetyl cysteine and acetyl-*L*-carnitine have been considered as available strategies for treating various inflammatory diseases [19]. However, these drugs still face the great challenges in the clinical treatment of ROS-related diseases for either of poor bioavailability, instability or low efficacy.

Attributed to the advances in nanotechnology, many new pathways for scavenging of ROS and treatment of ROS-related diseases have been developed by using various functional nanomaterials [20–23]. For instance, ultra-small and shape-diverse ceria nanoparticles [24, 25], ceria–zirconia nanoparticles [26], boron cluster-containing redox nanoparticles [27], eumelanin polymers [28], melanin polymers [29] and polydopamine nanoparticles [30] were applied for the scavenger of ROS. Other biopolymers of polystyrene [31], selenium-doped carbon quantum dots [32] and hydrophilic carbon clusters [33] were also developed for this domain. Recently, a great number of research interests have been focused on the construction of artificial nanozymes to mimic intracellular antioxidant enzyme to defend the oxidative damage [34]. Nanozymes are nanomaterials with natural enzyme-like characteristics, and they are promising rising star to alternate natural enzymes [35]. During the past several years, a series of nanozymes with unique antioxidant natural enzyme-like properties have been designed and fabricated. For example, V$_2$O$_5$ nanowires [36], Prussian blue nanoparticles [37], Copper tannic acid coordination nanosheet [38], MnO$_2$ nanozymes [39], Mn$_3$O$_4$ nanozymes [40], and functionalized graphene quantum dots [41] have been developed for scavenging ROS. Naturally, catalase (CAT), superoxide dismutase (SOD) and glutathione peroxidase (GPx) work together to construct the intracellular antioxidant system, and they display high

efficiency for broad-spectrum scavenging of ROS [42]. Based on the principle, the scientists have developed various nanozymes-ROS defense system which can provide CAT-like, SOD-like or GPx-like enzyme activity. A vanadia-based nanozyme represents a good sample to mimic a cellular antioxidant multienzyme system [43]. However, most of the reported nanozymes possess only one or two kinds of specific antioxidant activity, which is not enough for the prevention of oxidative stress. Thus, the developed nanozyme systems can't satisfactorily protect cell against oxidative damage [44]. It is highly desirable to develop innovative multienzyme mimetics to treat target ROS simultaneously. With the development of nanotechnology, the advanced nanozymes that are modularly designed are inspiringly emerging [45, 46]. However, to the best of our knowledge, no work has been reported about the fabrication of highly ordered multi-shelled nanocomposites as the highly integrated multienzyme mimetics-based antioxidation system.

Herein, inspired by the natural multienzyme systems and the urgently needed status for scavenging of intracellular ROS, a highly integrated core–shell nanocomposite is designed and synthesized. Through the developed simple radical polymerization and the *in-situ* oxidation-reduction reaction method, the well-designed multi-shelled manganese dioxide encapsulated selenium-melanin (Se@Me@MnO$_2$) nanocomposites are fabricated (Scheme 1). The *in vitro* experimental results showed that the Se@Me@MnO$_2$ nanocomposite is a powerful multienzyme mimetic to scavenge the H$_2$O$_2$, HO$^•$ and O$_2^{•-}$ through the CAT-like, SOD-like and GPx-like catalytic mechanisms. It exhibits high efficiency for intracellular antioxidation. In-depth mechanism investigation showed that the Se core possess GPx-like catalytic activity, the MnO$_2$ and the Me possess both the SOD-like and the CAT-like activities. The *in vivo* experiments showed that the harmful oxidative stress has been efficiently retarded and the inflammation was obviously alleviated. The developed ROS defense system takes the following advantages: (i) the Se@Me@MnO$_2$ nanozyme exhibits robust effects on scavenging diverse ROS, such as H$_2$O$_2$, HO$^•$ and O$_2^{•-}$; (ii) the Se@Me@MnO$_2$ nanozymes encompass the antioxidative ability of CAT-like, SOD-like and GPx-like to resist oxidative stress damage; (iii) it is capable to block ROS-triggered inflammatory activation; and (iv) the Se@Me@MnO$_2$ nanozymes have good biocompatibility. The newly developed Se@Me@MnO$_2$ nanocomposite is an ideal antioxidation nanozyme and have a good potential for further
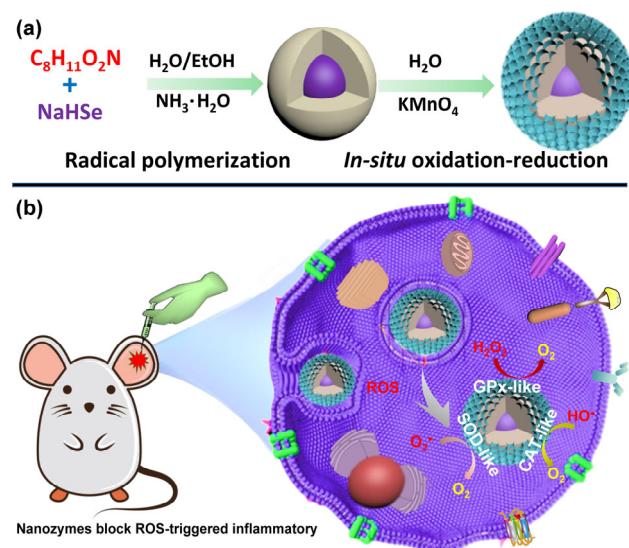
marketization.

2 Experimental

2.1 Synthesis of Se@Me@MnO$_2$ nanocomposites

2.1.1 Synthesis of NaHSe solution

The NaHSe was fabricated as Xie et al. [47]. The NaHSe aqueous solution was prepared via a reduction of Se and NaBH$_4$ in water under Ar. Firstly, 5 mL ultra-pure water was added into a flask and treated by ice bath. Followingly, 40 mg NaBH$_4$ was added and the Ar gas was used to exclude air. After that, 18 mg Se powder was added into the above solution and stirred for about 1 h. The reaction solution turns to transparent, then the NaHSe was synthesized.

2.1.2 Synthesis of Se@Me nanoparticles

The typical procedure for the fabrication of Se@Me nanoparticles was described as follows. In a round bottom flask, ethanol (40 mL), deionized water (90 mL) and ammonia aqueous (3 mL) was mixed and stirred for 15 min. Then 10 mL dopamine hydrochloride solution (2.6 mmol/mL) was injected into the above mixture solution drop by drop. After that, 2 mL NaHSe solution was added. The color of this solution immediately turned to pale yellow and gradually changed to dark brown. After stirred for 36 h, the reaction solution was centrifuged and the residues was washed with water for three times. Then the dark brown products were redispersed in 10 mL water for further use.

2.1.3 Synthesis of Se@Me@MnO$_2$ NPs nanozyme

The Se@Me@MnO$_2$ nanozyme were prepared through the oxidation-reduction reaction between the reductive carbon shell of Se@Me and the oxidative KMnO$_4$. In a typical experiment, 1 mL KMnO$_4$ aqueous solutions (8 mg/mL) were added to 10 mL Se@Me aqueous solution quickly, then the mixed solution was stirred at room temperature for 12 h. The Se@Me@MnO$_2$ nanozyme was washed with deionized water for three times and separated by centrifugation. The anticipate nanozyme was obtained by freeze-drying.

2.2 Scavenging of ROS

2.2.1 Scavenging of HO$^•$

HO$^•$ scavenging efficiency of Se@Me@MnO$_2$ nanozyme was measured with the response of fluorescent 2-hydroxyterephthalic acid. Solutions containing terephthalate (TA, 0.5 mM), H$_2$O$_2$ (10 mM), and Se@Me@MnO$_2$ nanozyme were prepared in phosphate buffer saline (PBS) (25 mM, pH 7.4). TA is a nonfluorescent compound that could capture HO$^•$ to produce 2-hydroxyterephthalic acid (*Ex*: 320 nm and *Em*: 425 nm). The mixtures were incubated for another 12 h and measured via fluorescence analysis.

2.2.2 Scavenging of H$_2$O$_2$

To investigate the GPx-like catalytic activity of the Se@Me@MnO$_2$ nanozyme, the following process was conducted. Se@Me@MnO$_2$ (0.05 mg/mL), glutathione (GSH, 2 mM), nicotinamide adenine dinucleotide phosphate (NADPH, 0.4 mM), glutathione reductase (GR, 1.7 units), and H$_2$O$_2$ (240 μM) were added into the PBS solution in order at room temperature. Then, different concentration of Se@Me@MnO$_2$ were added into the above solution. The steady-state kinetics of Se@Me@MnO$_2$ nanozyme was studied by varying the concentration of Se@Me@MnO$_2$ (0–0.05 mg/mL), at the fixed concentration of GR and NADPH in 25 mM pH 7.4 PBS. The reaction solution was detected by a UV–visible (UV–vis) spectrophotometer at 340 nm.

Scheme 1 (a) Schematic illustration for the fabrication of Se@Me@MnO$_2$ nanozyme. (b) Scavenging of inflammation induced intracellular ROS by the Se@Me@MnO$_2$ nanozyme.

2.2.3 Scavenging of $O_2^{\bullet-}$

$O_2^{\bullet-}$ scavenging efficiency of Se@Me@MnO$_2$ was achieved by measuring the inhibition ratio of photoreduction of NBT. The solutions containing riboflavin (20 μM), methionine (12.5 mM), nitrotetrazolium blue chloride (NBT, 75 μM), and Se@Me@MnO$_2$ nanozyme were prepared in PBS (25 mM, pH 7.4). The mixtures were illuminated upon ultraviolet radiation for 15 min. After illumination, the absorbances of mixtures were measured. Sample containing riboflavin, methionine, and NBT was defined as negative control. Sample containing riboflavin, methionine, and NBT after illumination was defined as positive control. All the experiments were carried out in dark without illumination. Inhibition percentage was calculated as the following formula: inhibition ratio = $[(A_0 - A_n)/(A_p - A_n)] \times 100\%$. A_0, A_n, and A_p were the absorbance of the treated samples, negative control, and positive control, respectively.

2.2.4 Electron paramagnetic resonance (EPR) test

The efficiency of the Se@Me@MnO$_2$ for scavenging of HO$^\bullet$ was further assessed with the EPR spectroscopy. In the general step, the H$_2$O$_2$ and the Se@Me@MnO$_2$ nanozyme were added into the PBS solution to obtain the pre-solution with 5 mmol/L H$_2$O$_2$ and 0.5 mg/mL Se@Me@MnO$_2$, and we took 5 mL for detection each time. The 5,5-dimethyl-1-pyrrolineN-oxide (DMPO) was applied to capture HO$^\bullet$. After exposure to ultraviolet light for 3 min, the adducts DMPO-HO$^\bullet$ were collected and detected by the EPR.

2.3 Cell cytotoxicity

The cytotoxicity of the Se@Me@MnO$_2$ nanozyme was verified by the Calcein-AM/PI double staining live/dead cells. Briefly, cells were firstly seeded with a density of 10^4 cells/well (100 μL total volume/well) in 96-well assay plates for 12 h. Then, Se@Me@MnO$_2$ nanozyme was added to the cell culture medium to form a series of cell culture medium with different concentrations (200 μg/mL, 100 μg/mL, 50 μg/mL, 25 μg/mL, 0 μg/mL). After incubated cells with the Se@Me@MnO$_2$ nanozyme for 24 h, the medium was removed and was washed by PBS. Then, the buffer solution containing Calcein-AM and PI was added into the 96-well assay plates and incubated for 30 min. After rewashing cells with PBS, the fluorescence microscopy was applied for the detection of the live/dead cell. Live cells are shown with green fluorescent (Excitation (Ex) = 490 nm, Emission (Em) = 515 nm) and the dead cells are displayed with red fluorescent (Ex = 530 nm, Em = 580 nm).

2.4 Intracellular ROS scavenging

2.4.1 Protective effect of Se@Me@MnO$_2$ to cells from oxidative stress

To investigate the efficiency of the Se@Me@MnO$_2$ on protecting cells from oxidative stress, the following research was conducted. Firstly, HepG2 cells were plated in a 6-well plate with a density of 10^4 per well for 12 h. After the medium was removed, cells were incubated with DMEM containing FBS (10%) and Se@Me@MnO$_2$ nanozyme (200 μg/mL, 100 μg/mL, 50 μg/mL, 25 μg/mL, 0 μg/mL) for 6 h, then the cells were washed with PBS solution to remove excessive Se@Me@MnO$_2$ nanozyme. Followingly, they were incubated with DMEM containing FBS (10%) and 5 mM H$_2$O$_2$ for 1 h. Finally, the cells live/dead ration were calculated through the Calcein-AM/PI double staining method as the same step of in 2.3. cell cytotoxicity assays.

2.4.2 Scavenging of the intracellular elevated ROS produced by Rosup treatment

Cells were first plated in a 6-well plate with a density of 10^4 per

well for 24 h. After the remove of the normal cell medium, another medium with different concentrations of Se@Me@MnO$_2$ nanozyme (100 μg/mL) was further used to culture cells for 12 h. As to treat cells by Rosup Kit, the Se@Me@MnO$_2$ nanozyme contained cell medium was removed and further washed with PBS for 3 times. Following, cell medium includes DCFH-DA was used to cultivate cells for 1 h. After the probes were successfully loaded, mediums were removed and cells were washed by PBS for 3 times. After that, cell mediums including Rosup were used to cultivate cells for 1 h. Group without any treatment was defined as control. Fluorescence microscopy images were collected on an Olympus imaging system (Ex = 488 nm, Em = 525 nm). For the quantitative results, cells were subjected to flow cytometry (n =3).

2.5 Inflammation models

Kunming mice (3 × 8) weighting about 20 g were achieved from Experimental Animal Center of Tsinghua University. During the protocol, mouse hair was first removed, then 10 μL phorbol 12-myristate 13-acetate solution (PMA, 100 μg/mL in acetone) was injected into the ear of the mouse. After 6 h, mouse with the local ear inflammation was obtained. After that, 50 μg/mL different nanomaterials (MnO$_2$, Me, Se@Me MnO$_2$, and Se@Me@MnO$_2$ nanozyme) were injected into different mice respectively. Subsequently, fluorescence imaging of mice was acquired 30 min after subcutaneous (s.c.) injection of DCFH-DA solution. The degree of inflammation can be clearly recognized by the black color of the mouse ears. In addition, the frozen section fluorescence experiment was used to further verify the experimental results. In the slice experiment, we first took the skin tissue from the injected ear of the root and frozen after OCT embedding. Then, we added diluted 4′,6-diamidino-2-phenylindole (DAPI) and incubated at room temperature for 10 min. Furthermore, we are covering each slide with an appropriate amount of anti-fluorescence quencher and observed the distribution of fluorescence with a fluorescence microscope. The photoluminescence pictures were further treated by the ImageJ to obtain the relative fluorescence intensity data. Experiments were performed according to the established animal protocols and guidelines approved by the Ethics Review Committee on Animal Experimentation of Tsinghua University (Beijing, China).

3 Results and discussion

In order to fabricate the Se@Me@MnO$_2$ nanocomposites, the dopamine was firstly polymerized in the EtOH/water blending solution under alkaline condition, at the same time, the NaHSe solution was added into the reaction mixture to synthesize the Se@Me. Then, the Se@Me@MnO$_2$ were prepared through the oxidation-reduction reaction between the reductive carbon shell of Se@Me and the oxidative KMnO$_4$. The synthesis of Se@Me and Se@Me@MnO$_2$ were conducted at room temperature. In order to observe the morphology changes of the Se@Me@MnO$_2$, the field-emission scanning electron microscopy (FESEM), transmission electron microscopy (TEM) and high-resolution transmission electron microscopy (HR-TEM) were all applied to characterize the intermediates that produced during the preparation process. The FESEM and TEM images demonstrated that the fabricated Se@Me was uniform and the average size is about 100 nm ((Fig. 1(a) and Figs. S1(a) and S1(b) in the Electronic Supplementary Material (ESM)). Furthermore, the Se was located at the core position with about 20 nm (Figs. S1(c) and S1(d) in the ESM). This result was attributed to the self-agglomeration of selenium nanoparticles when dopamine polymerized. Through the FESEM and HR-TEM characterizations
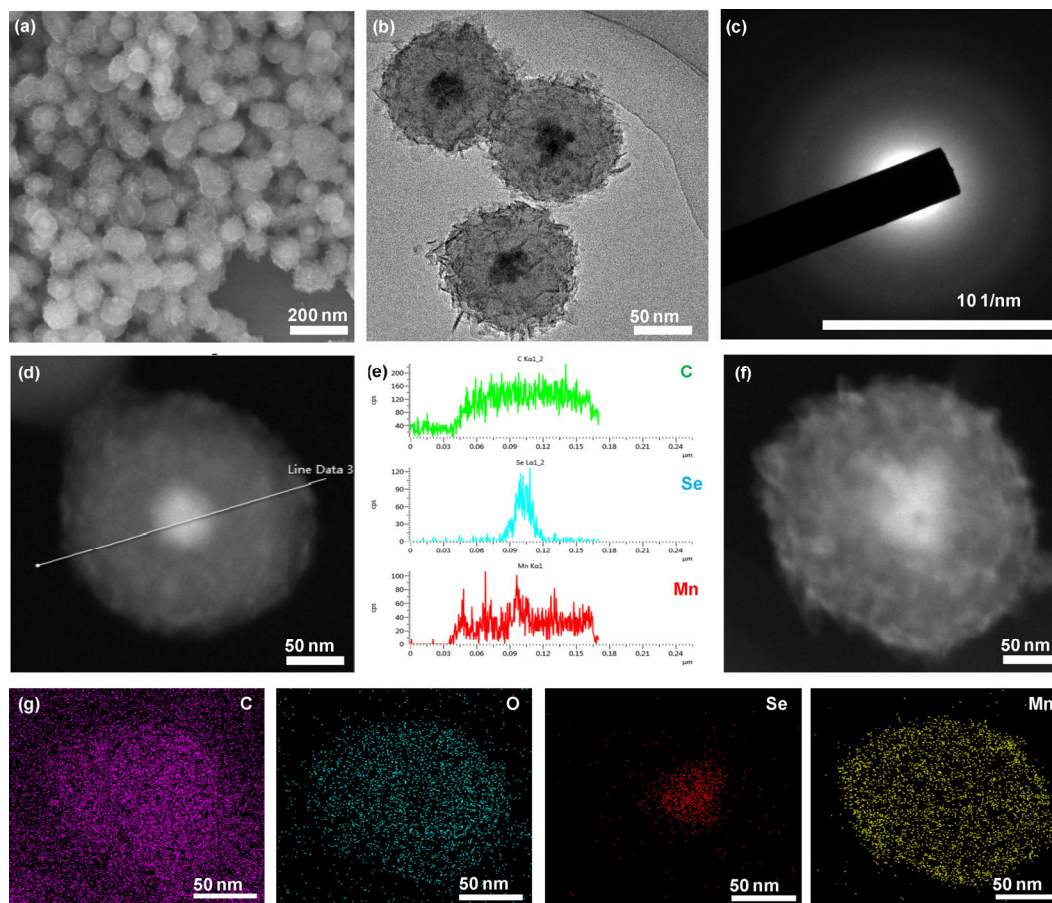
Figure 1 (a) FESEM image, (b) HR-TEM image, (c) SAED pattern, (d) and (e) Line scanning, (f) STEM, (g) EDX elemental mapping of Se@Me@MnO$_2$ nanocomposites.

of the as-synthesized Se@Me@MnO$_2$, the MnO$_2$ outer shell encapsulated the Se@Me and the average size of the Se@Me@MnO$_2$ is about 150 nm (Fig. 1(b) and Fig. S2 in the ESM). From the intermediate products, it is obvious that the MnO$_2$ were grown gradually on the Me shell layer (Fig. S3 in the ESM). Furthermore, the images have shown a clear morphology of the uniform multi-shelled Se@Me@MnO$_2$ nanocomposite. The selected area electron diffraction (SAED) characterization illustrated that the Se@Me@MnO$_2$ is amorphous (Fig. 1(c)). We selected a Se@Me@MnO$_2$ nanocomposite to investigate the elements dispersion by the line-scanning spectra characterization (Figs. 1(d) and 1(e)). The line-scanning result obviously shown that Se, Me and MnO$_2$ exist as layer by layer nanostructure. The MnO$_2$ layer was about 15–20 nm. Further combining with the results of scanning transmission electron microscopy (STEM) and the energy-dispersive X-ray (EDX) spectroscopy-elemental mapping spectra (Figs. 1(f) and 1(g), Figs. S4 and S5 in the ESM), the distribution of elements C, O, Mn and Se were clearly visible and the corresponding mass of these elements is 74.9%, 15.0%, 2.6% and 1.4%. The above characterizations of the obtained nanomaterials demonstrated that the designed structure of the Se@Me@MnO$_2$ has been successfully fabricated.

The Fourier transform infrared spectrum (FT-IR) was used to investigate the reaction process by the changes of functional group. As shown in Fig. 2(a), the peaks intensity of free OH– and NH$_2$– groups gradually decreased, which means the dopamine was polymerized to Me. The FT-IR of the Se@Me was like the Me, which demonstrates the Se was encapsulated by the Me, therefore, it possesses excellent water-soluble ability just like the Me itself. From the spectrum of Se@Me@MnO$_2$, the change of the spectrum image illustrates the MnO$_2$ have encapsulated Se@Me successfully, and the water solubility of

the finally fabricated nanocomposite decreased slightly. The UV–vis spectrophotometer was applied to explore the change law of absorbance of this material with concentration. It is obvious that the Se@Me@MnO$_2$ solution appears absorbance in near infrared region and the absorbance is proportional to concentration, and the phenomenon indicate that this material has potential as a photothermal material (Fig. 2(b) and Fig. S6 in the ESM). The stability of the nanocomposite was tested by the ζ potential characterization. As the MnO$_2$ nanosheets growth on the Se@Me, the ζ potential increased from −62 to −24 mV (Fig. 2(c)). This result suggests the stability of the Se@Me@MnO$_2$ was decreased as the Se@Me encapsulated by the MnO$_2$ and it could be gradually degraded during metabolism *in vivo*. The crystal structure of the Se@Me@MnO$_2$ was confirmed by the powder X-ray diffraction (XRD). The XRD pattern doesn't show any sharp peaks and the result further confirmed that the Se@Me@MnO$_2$ is amorphous (Fig. S7 in the ESM) [48]. The nitrogen adsorption and desorption experiment demonstrate the adsorption/desorption isotherm of the Se@Me@MnO$_2$ nanoparticles belongs to type IV. What's more, the major pore sizes of the nanoparticles are below 10 nm (Figs. S8 and S9 in the ESM). The element valence of the fabricated nanocomposites was confirmed by the X-ray photoelectron spectroscopy (XPS) (Figs. 2(d)–2(i)). Based on the XPS survey spectroscopy, the nanocomposites contain C, N, O, Se and Mn and the corresponding peaks of C 1s, N 1s, O 1s, Se 3d and Mn 2p display in the survey spectrum. The C 1s spectrum exhibits peaks at the binding energy of 284.2, 286.1 and 287.3 eV, which are corresponding to the C–C/C=C, C–O–C and C=O, respectively. The N 1s XPS spectra show a sharp single peak at the 399.7 eV, which is attributed to the C–N from the Me. Furthermore, the O 1s spectrum illustrates the presence of
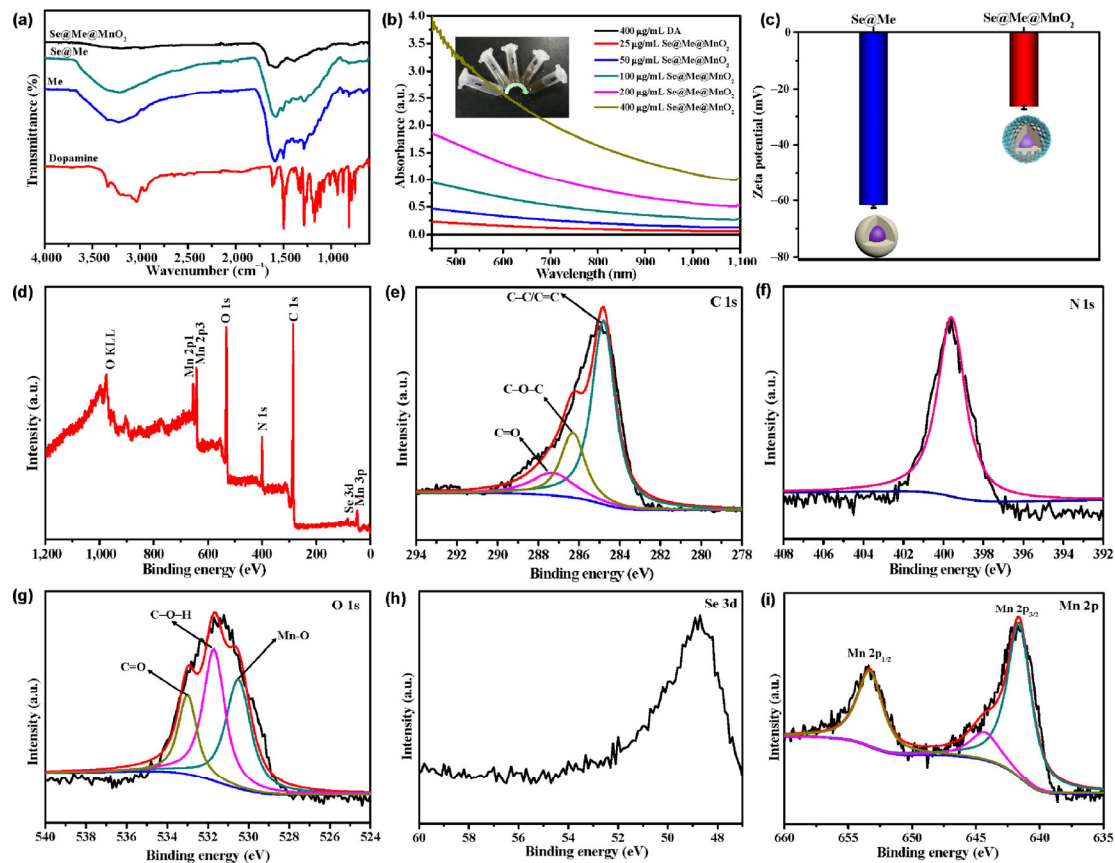
Figure 2 (a) Fourier transform infrared (FT-IR) spectroscopy of dopamine, Me, Se@Me, and Se@Me@MnO₂. (b) UV–vis absorption spectra of Se@Me@MnO₂ with different concentrations. (c) Zeta (ζ) potentials of Se@Me and Se@Me@MnO₂. (d) Survey X-ray photoelectron spectroscopy (XPS) spectrum of Se@Me@MnO₂. (e) XPS spectrum of the C 1s region. (f) XPS spectrum of the N 1s region. (g) XPS spectrum of the O 1s region. (h) XPS spectrum of the Se 3d region. (i) XPS spectrum of the Mn 2p region.

C=O (532.8 eV), C–O–H (531.2 eV), and Mn–O (530.1 eV) groups. The Se 3d spectrum reveals the presence of Se–Se and Se–C in the nanocomposites. This is attributed to the dopamine undergoes free radical polymerization, the oxidizing free radicals oxidize the negatively divalent selenium to Se–Se and Se–C status [47]. Furthermore, from the Mn 2p spectra, the binding energy of Mn $2p_{3/2}$ and Mn $2p_{1/2}$ was corresponding to 642.6 and 653.1 eV, respectively, which means the Mn exists as MnO₂ [49, 50].

The as synthesized Se@Me@MnO₂ nanocomposites were utilized as enzyme mimetic to investigate the ability of ROS scavenging. Firstly, the H₂O₂ was used as the HO˙ precursor to test the scavenging efficiency of Se@Me@MnO₂ nanocomposites. In this procedure, the scavenging efficiency was achieved by measuring the presence of fluorescent 2-hydroxyterephthalic acid. As shown in Fig. 3(a), the result demonstrates in the presence of 100 μg/mL Se@Me@MnO₂ NPs, about 97% HO˙ have been scavenged (Fig. 3(b)). The result means that with the assistance of Se@Me@MnO₂, the HO˙ can be effectively eliminated with CAT-like pathway. What's more, the EPR spectroscopy was used to confirm the ability of Se@Me@MnO₂ nanocomposites to scavenge HO˙. As shown in Fig. 3(c), after the H₂O₂ irradiated by the UV for 3 min, a strong EPR signal appears, which indicated the formation of the DEMPO/HO˙ adduct. On the other hand, after excluding other factors, as the Se@Me@MnO₂ was added into the H₂O₂, it is obvious that the ESR signals of the DEMPO/HO˙ adduct disappeared. The results confirmed that the Se@Me@MnO₂ nanocomposites had strong HO˙ scavenging ability. Furthermore, the durability is an important indicator for enzymes. Therefore, we further investigated the stability of Se@Me@MnO₂ to scavenge HO˙.

As the Fig. S10(a) in the ESM shown, the Se@Me@MnO₂ can be used more than 6 times for the removal of HO˙ with over 95% clearance rate. What's more, the stability of Se@Me@MnO₂ to scavenge HO˙ in cell culture medium was also investigated. As shown in the Fig. S10(b) in the ESM, the result demonstrated that the nanozyme has good stability in the culture medium. The reused nanozymes were further conducted by the FESEM and TEM characterizations to confirm the morphology and structure stability. As shown in Fig. S11 in the ESM, the morphology of the reused nanozymes dose not show significant change, which further confirmed the nanozymes are highly stable. Inspired by the above results, we further investigate the Se@Me@MnO₂ nanocomposites GPx-like and the SOD-like enzyme activity. To investigate the GPx-like enzyme activity, the NADPH UV–vis absorption spectrum has been real-timely monitored at 340 nm wavelength. As shown in Fig. 3(d), for the situations of without H₂O₂ or without GSH, the NADPH absorption curves have not shown obvious decrease. After the addition of the Se@Me@MnO₂ nanocomposites, an obvious decrease of NADPH concentration was observed. Furthermore, from the concentration controlling experiment, an obvious NADPH concentration decreases with the increase of the Se@Me@MnO₂ nanocomposites as shown in Fig. 3(e). The above results indicated the Se@Me@MnO₂ nanocomposite have high GPx-like enzyme activity to remove excess H₂O₂. As one of the significant antioxidant enzymes in organisms, the SOD can catalyze the disproportionation serving. In order to explore the SOD-like enzyme activity of the Se@Me@MnO₂ nano-composites, we conducted the O₂˙⁻ scavenging protocol. The scavenging efficiency of Se@Me@MnO₂ was achieved by measuring the inhibition ratio of photoreduction of nitrotetrazolium
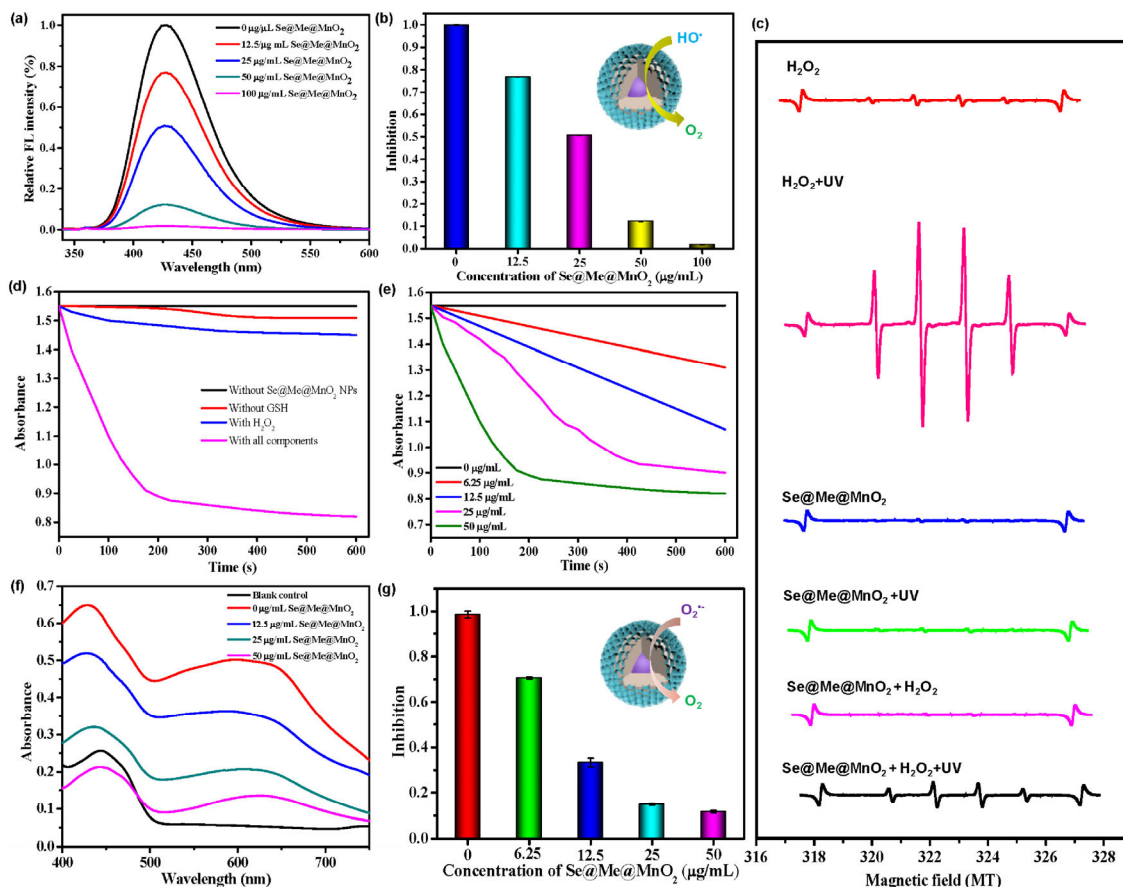
Figure 3 Antioxidant enzyme-like properties of nanocomposites: (a) Scavenging of HO$^\bullet$ with different concentration of Se@Me@MnO$_2$ nanocomposites. (b) Percent inhibition of terephthalate oxidation with different concentrations of nanocomposites. (c) EPR spectra of DMPO/$^\bullet$OH adducts were collected after incubation for 3 min with different samples. (d) The Se@Me@MnO$_2$ nanocomposites scavenges H$_2$O$_2$ through GPx-like mechanism. (e) Time-dependent absorbance changes of NADPH with different concentrations of Se@Me@MnO$_2$ nanocomposites. (f) Scavenging efficiency of superoxide radicals. (g) Percent inhibition of NBT oxidation with different concentrations of Se@Me@MnO$_2$ nanocomposites.

blue chloride (NBT). Phosphate buffer saline solutions containing riboflavin, methionine, NBT, and Se@Me@MnO$_2$ nanocomposites were first prepared. Then the mixtures were illuminated upon ultraviolet radiation. After that, the visible spectrum absorbances of mixtures were measured. As shown in Fig. 3(f), the absorption peaks at 560 nm decrease with different concentrations of Se@Me@MnO$_2$ nanocomposites. The result means the produced O$_2$$^{\bullet-}$ have been scavenged by the Se@Me@MnO$_2$ nanocomposites through the SOD-like enzyme catalysis route. What's more, about 90% O$_2$$^{\bullet-}$ have been cleared in the presence of 50 μg/mL nanozyme (Fig. 3(g)).

Although the Se@Me@MnO$_2$ nanocomposites possess the CAT-like, GPx-like and the SOD-like enzyme activities, it is essential to reveal the respective role in scavenge ROS, namely, the inner link of Me, Se@Me and MnO$_2$. Thus, the fabricated Me nanoparticles, Se@Me nanoparticles, and MnO$_2$ nanoparticles were applied to scavenging ROS. We conducted the experimental research which same to Se@Me@MnO$_2$ nanocomposites to scavenge ROS. According to the research results, the MnO$_2$ nanoparticles and the Me nanoparticles have been proved to possess both the SOD-like and the CAT-like mimic activities and can scavenge O$_2$$^{\bullet-}$ and $^\bullet$OH (Figs. S12 and S14 in the ESM). And the Se@Me possess the CAT-like, GPx-like and the SOD-like enzyme activities (Fig. S13 in the ESM), which means the Se core possess GPx-like catalytic activity. Thus, for catalytic mechanism of the Se@Me@MnO$_2$ nanozyme, the outer layer MnO$_2$ and the middle layer Me are SOD-like and the CAT-like enzyme mimics, the Se core is GPx-like enzyme mimic. Furthermore, the experimental data clearly shows

that whether the Me, Se@Me, or MnO$_2$, their corresponding active oxygen scavenging ability is insufficient. In addition, for the Se@Me@MnO$_2$ nanocomposites, the enzyme catalytic activity is not a simple addition of the catalytic activities of Se, Me, and MnO$_2$. For the Se@Me@MnO$_2$ nanozyme, the ROS scavenging activity shows significant increase, which indicates that the three components of the Se@Me@MnO$_2$ nanozyme synergistically catalyzed ROS scavenging. The above result may attribute to the large number of stable unpaired electrons exist in the nanocomposites, the Se, Me and MnO$_2$ provide synergistic and fast electron transfer effect during the process of scavenging ROS, and achieving the quickly remove of ROS.

The newly developed Se@Me@MnO$_2$ nanozyme were further utilized for antioxidation in cellular microenvironment to protect the body against oxidative stress. Before that, in order to investigate the biocompatibility of the Se@Me@MnO$_2$ nanozyme, we firstly test the cytotoxicity of the nanozyme by three kinds of cells: HepG2 cells (a human liver carcinoma cell line), A549 cells (a human lung adenocarcinoma cell line) and SK-MES-1 cells (a human lung squamous cell line). As shown in Fig. 4(a) and Fig. S15 in the ESM, the experimental results about cell live/death illustrated that although co-incubating these three kinds of cells with a series of concentrations (0, 100, 200 μg/mL) of nanozyme for 24 h, no obvious inhibiting effect on cell proliferation was observed. This result demonstrates our system possess good biocompatibility and could be practical for further biological usages. It is well known the oxidative stress was occurred when excess ROS can't be removed timely, and the oxidative stress will lead to cell death.
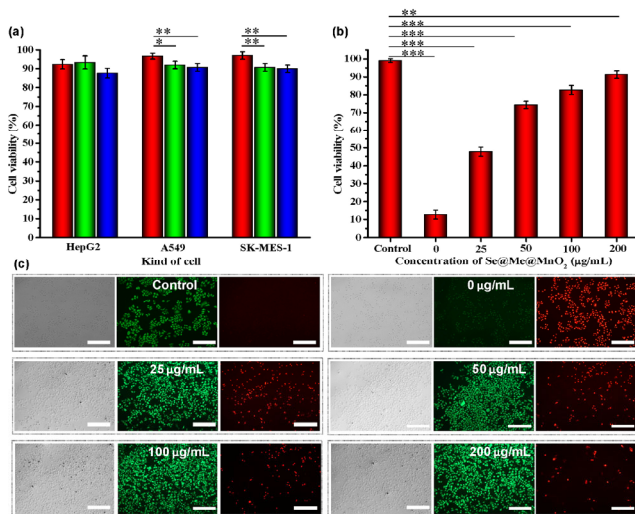
Figure 4 (a) Cell viability of HepG2 cells, A549 cells and SK-MES-1 cells incubated with different concentrations of Se@Me@MnO₂ for 24 h. (Red column represents control group, green column represents 100 μg/mL, blue column represents 200 μg/mL; all data are expressed as the mean ± standard error of the mean (s.e.m.). $*p < 0.05$, $**p < 0.01$ when compared with control group, $n = 3$. (b) The protective effect of Se@Me@MnO₂ to HepG2 cells from oxidative stress; all data are expressed as the mean ± s.e.m. $**p < 0.01$, $***p < 0.001$ when compared with control group, $n = 3$. (c) Fluorescence microscopy images of HepG2 cells that protect by the Se@Me@MnO₂ from oxidative stress (Scale bar is 100 μm).

In order to investigate the effects of Se@Me@MnO₂ nanozyme on oxidative stress that can induce cell death *in vitro*, the cell tests were conducted. As shown in Figs. 4(b) and 4(c), based on the cell live/death experiment through the Calcein-AM/PI double staining method, the Se@Me@MnO₂ nanozyme exhibits satisfactory ability to protect HepG2 cells from H₂O₂ treatment. The cell images obviously demonstrated that without the Se@Me@MnO₂ nanozyme, about 90% cell died. However, as the HepG2 cells treated with the 0–200 μg/mL Se@Me@MnO₂ nanozyme, the cell death caused by H₂O₂ was decreased. After that, we further investigated the intracellular antioxidant

capacity of the Se@Me@MnO₂ nanozyme.

For the purpose to survey intracellular ROS scavenging ability of the Se@Me@MnO₂ nanozyme, the HepG2 cells were firstly co-cultured with the Se@Me@MnO₂ nanocomposites for 12 h, and then treated with Rosup kit. During the procedure, the HepG2 cells treated by nanocomposites were firstly loaded on the DCFH-DA fluorescence probe and then the medium contained Rosup ingredient was used to treat the HepG2 cells. The intracellular ROS level could be monitored by using DCFH-DA as the fluorescence probe. As shown in Figs. 5(a) and 5(b), the fluorescence intensity of DCFH-DA significantly reduced when the Se@Me@MnO₂ were added to the system.

Furthermore, in order to quantitatively analyze the Rosup induced ROS generation and the Se@Me@MnO₂ nanozyme caused ROS scavenging, the flow cytometry analysis was conducted. As shown in Fig. 5(c), about 60% ROS could be removed efficiently. This suggested that the Se@Me@MnO₂ nanozyme is a well-done ROS scavenger and can protect the cells from oxidative stress damage.

In order to examine the potential application of this antioxidant system in block ROS-triggered inflammation, the ear inflammation model of Kunming mouse has been constructed and treated by the Se@Me@MnO₂ nanozyme. To obtain the ear inflamed mouse model, the phorbol 12-myristate 13-acetate (PMA) has been injected into the mouse ear. After injecting PMA for 6 h, as shown in Fig. 6(a)(i)-(ii), the mouse ear turned to black color. When PMA was injected into mice, the color of the mice skin change to black due to melanosis after inflammation. This is a common phenomenon after skin inflammation. Studies have found that after inflammation, the skin barrier function is impaired, and the density of melanocytes in the affected area usually increases. This phenomenon indicates the *in vivo* inflammation animal model was obtained. To study the ROS removal capability of our nanocomposites against inflammation, the ears were treated by the Se@Me@MnO₂ nanozyme with different concentrations and the DCFH-DA solution was injected by subcutaneous (s.c.). As demonstrated in Fig. 6(a)(iii)–(v), 30 min later, with the assistance of the Se@Me@MnO₂ nanozyme, the black color part of the mouse ear
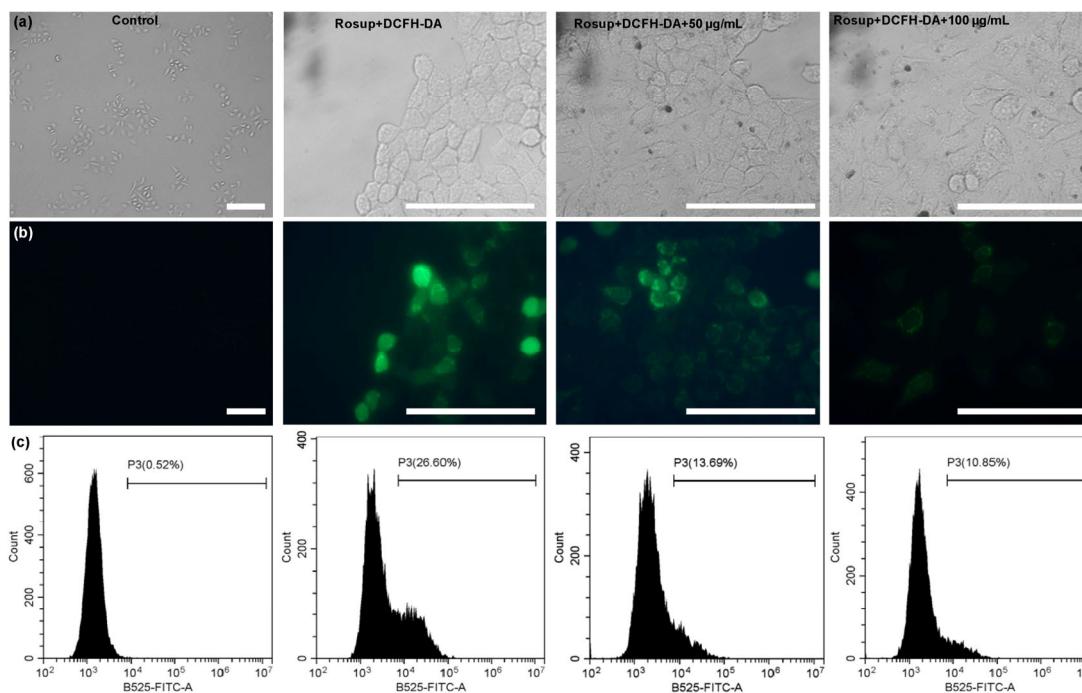

Figure 5 (a) and (b) Fluorescence microscopy images of HepG2 cells with the treatment of Se@Me@MnO₂ nanozyme. (c) Flow cytometry analysis used to monitor the changes of intracellular ROS (scale bar is 100 μm).
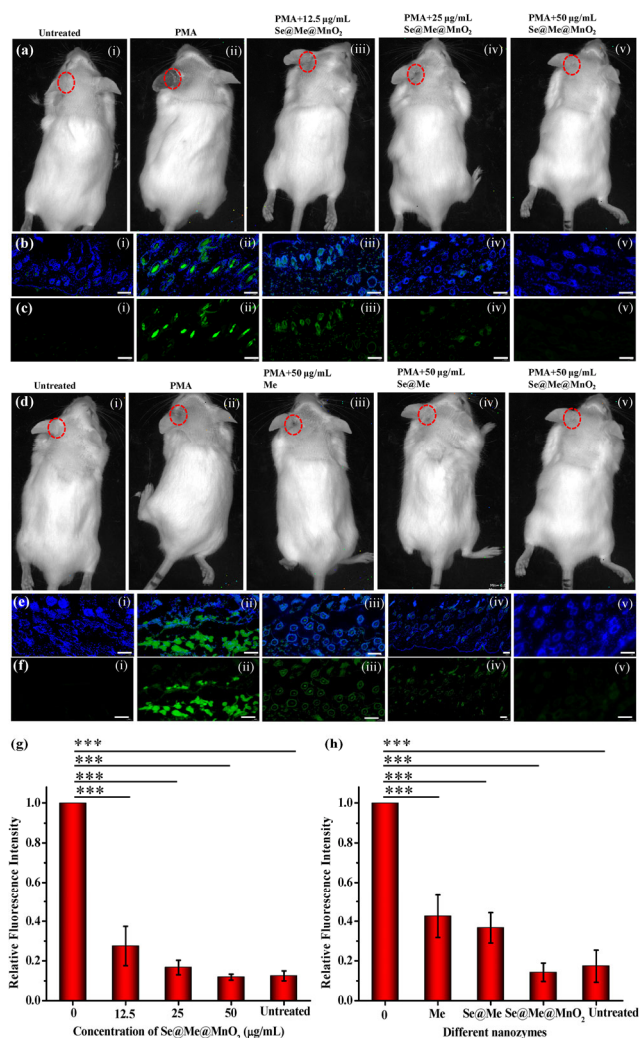
Figure 6 (a) The effects of Se@Me@MnO₂ nanozyme on scavenging of ROS *in vivo* ear inflammation mice. ((b) and (c)) Frozen sections fluorescence pictures of mouse ears treated by different concentrations Se@Me@MnO₂ nanozyme, green fluorescence comes from the reaction between ROS and DCFH-DA. (d) The effects of Se, Se@Me and Se@Me@MnO₂ nanozyme on scavenging of ROS *in vivo* ear inflammation mice. ((e) and (f)) Frozen sections fluorescence pictures of mouse ears treated by Se, Se@Me and Se@Me@MnO₂ nanozyme, green fluorescence comes from the reaction between ROS and DCFH-DA. The scale bar is 100 μm. (g) The relative fluorescence intensity of frozen sections of mouse ears treated with Se@Me@MnO₂ nanocomposites at different concentrations, all data are expressed as the mean ± s.e.m. ***$p < 0.001$ when compared with control group, $n = 3$. (h) The relative fluorescence intensity of frozen sections of mouse ears treated by Se, Se@Me, and Se@Me@MnO₂ nanocomposites, all data are expressed as the mean ± s.e.m. ***$p < 0.001$ when compared with control group, $n = 3$.

gradually gets smaller, this means the inflammation intensity of the mouse ear decreased. When increasing the concentrations of the nanocomposites, the inflammation intensity decreased gradually. For the purpose of more intuitive and more convincing to illustrate the effect of the Se@Me@MnO₂ nanozyme on removing of ROS in inflammation, the frozen sections of the corresponding mouse ears have been used to observe the distribution of fluorescence by fluorescence microscope. As shown in Figs. 6(b) and 6(c) and Fig. S16 in the ESM, without the Se@Me@MnO₂ nanozyme, the green fluorescence of the ear inflamed mouse is very strong. Conversely, it is not so obvious in the Se@Me@MnO₂ nanozyme treated experimental groups, and the green fluorescence gradually weakened as the concentrations of the nanocomposites increased. The intensity

of green fluorescence was reduced as much as 90%, and the intensity of treatment group with the 50 μg/mL Se@Me@MnO₂ nanozyme has no significant difference to the untreated group (Fig. 6(g)). The fluorescence images of mouse ears frozen sections further confirmed that the Se@Me@MnO₂ nanozyme have a good ROS scavenging effect. What's more, Me nanocomposites, Se@Me nanocomposites and Se@Me@MnO₂ nanozyme were applied to scavenge ROS *in vivo* ear inflammation mice (Fig. 6(d)). Similarly, frozen sections are also used to test the results. As shown in Figs. 6(e) and 6(f) and Fig. S17 in the ESM, the experimental results illustrated the Se@Me@MnO₂ nanozyme exhibit the best performance than the Me nanocomposites, Se@Me nanozyme, which is consistant with the *in vitro* experimental result. The relative fluorescence intensity of mouse ears treated by Se, Se@Me, and Se@Me@MnO₂ nanozyme further proves the necessity of this highly integrated multilayer structure due to the synergy effect of the three components (Fig. 6(h)). All the above results indicated our system possessed excellent ROS removal capacity in the inflamed mouse model and might have potential application in inflammation therapy.

4 Conclusions

In conclusion, we have developed a simple method for the fabrication of Se@Me@MnO₂ nanocomposites. The Se@Me@MnO₂ nanocomposites possess SOD-like, CAT-like and GPx-like enzyme catalytic activities to protect the body against oxidative stress. For this biocompatible multifunctional nanozyme, the outer layer MnO₂ and the middle layer Me have been discovered to possess SOD-like and CAT-like mimic activities, and the Se core possesses GPx-like catalytic activity. The activity of Se@Me@MnO₂ nanozyme is attributed to the numerous stable unpaired electrons that exist in the nanocomposites, which offers synergistic and fast electron transfer effect during the process of scavenging ROS. Both the *in vitro* and *in vivo* experiments demonstrated that the fabricated nanocomposites exhibit excellent intracellular ROS removal ability to defend cell components against oxidative stress, and show potential in inflammation therapy.

References

[1] Noubade, R.; Wong, K.; Ota, N.; Rutz, S.; Eidenschenk, C.; Valdez, P. A.; Ding, J. B.; Peng, I.; Sebrell, A.; Caplazi, P. et al. NRROS negatively regulates reactive oxygen species during host defence and autoimmunity. *Nature* **2014**, *509*, 235–239.

[2] Yang, B. W.; Chen, Y.; Shi, J. L. Reactive oxygen species (ROS)-based nanomedicine. *Chem. Rev.* **2019**, *119*, 4881–4985.

[3] Gao, S. S.; Lin, H.; Zhang, H. X.; Yao, H. L.; Chen, Y.; Shi, J. L. Nanocatalytic tumor therapy by biomimetic dual inorganic nanozyme-catalyzed cascade reaction. *Adv. Sci.* **2019**, *6*, 1801733.

[4] Wang, Z. Z.; Zhang, Y.; Ju, E. G.; Liu, Z.; Cao, F. F.; Chen, Z. W.; Ren, J. S.; Qu, X. G. Biomimetic nanoflowers by self-assembly of

nanozymes to induce intracellular oxidative damage against hypoxic tumors. *Nat. Commun.* **2018**, *9*, 3334.

[5] Tong, L. Y.; Chuang, C. C.; Wu, S. Y.; Zuo, L. Reactive oxygen species in redox cancer therapy. *Cancer Lett.* **2015**, *367*, 18–25.

[6] Panieri, E.; Santoro, M. M. ROS homeostasis and metabolism: A dangerous liason in cancer cells. *Cell Death. Dis.* **2016**, *7*, e2253.

[7] Chouchani, E. T.; Kazak, L.; Jedrychowski, M. P.; Lu, G. Z.; Erickson, B. K.; Szpyt, J.; Pierce, K. A.; Laznik-Bogoslavski, D.; Vetrivelan, R.; Clish, C. B. et al. Mitochondrial ROS regulate thermogenic energy expenditure and sulfenylation of UCP1. *Nature* **2016**, *532*, 112–116.

[8] Zhao, Z. H.; Wang, W. Q.; Li, C. X.; Zhang, Y. Q.; Yu, T. R.; Wu, R. F.; Zhao, J. Y.; Liu, Z.; Liu, J.; Yu, H. J. Reactive oxygen species–activatable liposomes regulating hypoxic tumor microenvironment for synergistic photo/chemodynamic therapies. *Adv. Funct. Mater.* **2019**, *29*, 1905013.

[9] Houstis, N.; Rosen, E. D.; Lander, E. S. Reactive oxygen species have a causal role in multiple forms of insulin resistance. *Nature* **2006**, *440*, 944–948.

[10] Finkel, T.; Holbrook, N. J. Oxidants, oxidative stress and the biology of ageing. *Nature* **2000**, *408*, 239–247.

[11] Allen, C. L.; Bayraktutan, U. Oxidative stress and its role in the pathogenesis of ischaemic stroke. *Int. J. Stroke* **2009**, *4*, 461–470.

[12] Xu, X. D.; Saw, P. E.; Tao, W.; Li, Y. J.; Ji, X. Y.; Bhasin, S.; Liu, Y. L.; Ayyash, D.; Rasmussen, J.; Huo, M. et al. ROS-responsive polyprodrug nanoparticles for triggered drug delivery and effective cancer therapy. *Adv. Mater.* **2017**, *29*, 1700141.

[13] Bian, P. X.; Zhang, J. X.; Wang, J. Y.; Yang, J.; Wang, J. Y.; Liu, H. L.; Sun, Y. M.; Li, M. X.; Zhang, X. D. Enhanced catalysis of ultrasmall Au-MoS₂ clusters against reactive oxygen species for radiation protection. *Sci. Bull.* **2018**, *63*, 925–934.

[14] Imlay, J. A.; Linn, S. DNA damage and oxygen radical toxicity. *Science* **1988**, *240*, 1302–1309.

[15] Diehn, M.; Cho, R. W.; Lobo, N. A.; Kalisky, T.; Dorie, M. J.; Kulp, A. N.; Qian, D. L.; Lam, J. S.; Ailles, L. E.; Wong, M. et al. Association of reactive oxygen species levels and radioresistance in cancer stem cells. *Nature* **2009**, *458*, 780–783.

[16] Nathan, C.; Cunningham-Bussel, A. Beyond oxidative stress: An immunologist's guide to reactive oxygen species. *Nat. Rev. Immunol.* **2013**, *13*, 349–361.

[17] Puente, B. N.; Kimura, W.; Muralidhar, S. A.; Moon, J.; Amatruda, J. F.; Phelps, K. L.; Grinsfelder, D.; Rothermel, B. A.; Chen, R.; Garcia, J. A. et al. The oxygen-rich postnatal environment induces cardiomyocyte cell-cycle arrest through DNA damage response. *Cell* **2014**, *157*, 565–579.

[18] Roth, T. L.; Nayak, D.; Atanasijevic, T.; Koretsky, A. P.; Latour, L. L.; McGavern, D. B. Transcranial amelioration of inflammation and cell death after brain injury. *Nature* **2014**, *505*, 223–228.

[19] Liu, T. F.; Xiao, B. W.; Xiang, F.; Tan, J. L.; Chen, Z.; Zhang, X. R.; Wu, C. Z.; Mao, Z. W.; Luo, G. X.; Chen, X. Y. et al. Ultrasmall copper-based nanoparticles for reactive oxygen species scavenging and alleviation of inflammation related diseases. *Nat. Commun.* **2020**, *11*, 2788.

[20] Wu, J. J. X.; Wang, X. Y.; Wang, Q.; Lou, Z. P.; Li, S. R.; Zhu, Y. Y.; Qin, L.; Wei, H. Nanomaterials with enzyme-like characteristics (nanozymes): Next-generation artificial enzymes (II). *Chem. Soc. Rev.* **2019**, *48*, 1004–1076.

[21] Liu, Y. L.; Shi, J. J. Antioxidative nanomaterials and biomedical applications. *Nano Today* **2019**, *27*, 146–177.

[22] Zhu, X.; Radovic-Moreno, A. F.; Wu, J.; Langer, R.; Shi, J. J. Nanomedicine in the management of microbial infection-overview and perspectives. *Nano Today* **2014**, *9*, 478–498.

[23] Liu, X. L.; Pan, Y. C.; Yang, J. J.; Gao, Y. F.; Huang, T.; Luan, X. W.; Wang, Y. Z.; Song, Y. J. Gold nanoparticles doped metal-organic frameworks as near-infrared light-enhanced cascade nanozyme against hypoxic tumors. *Nano Res.* **2020**, *13*, 653–660.

[24] Kim, C. K.; Kim, T.; Choi, I. Y.; Soh, M.; Kim, D.; Kim, Y. J.; Jang, H.; Yang, H. S.; Kim, J. Y.; Park, H. K. et al. Ceria nanoparticles that can protect against ischemic stroke. *Angew. Chem., Int. Ed.* **2012**, *51*, 11039–11043.

[25] Li, Y. Y.; He, X.; Yin, J. J.; Ma, Y. H.; Zhang, P.; Li, J. Y.; Ding, Y. Y.; Zhang, J.; Zhao, Y. L.; Chai, Z. F. et al. Acquired superoxide-scavenging ability of ceria nanoparticles. *Angew. Chem., Int. Ed.* **2015**, *54*, 1832–1835.

[26] Soh, M.; Kang, D. W.; Jeong, H. G.; Kim, D.; Kim, D. Y.; Yang, W.; Song, C.; Baik, S.; Choi, I. Y.; Ki, S. K. et al. Ceria-zirconia nanoparticles as an enhanced multi-antioxidant for sepsis treatment. *Angew. Chem., Int. Ed.* **2017**, *56*, 11399–11403.

[27] Gao, Z. Y.; Horiguchi, Y.; Nakai, K.; Matsumura, A.; Suzuki, M.; Ono, K.; Nagasaki, Y. Use of boron cluster-containing redox nanoparticles with ROS scavenging ability in boron neutron capture therapy to achieve high therapeutic efficiency and low adverse effects. *Biomaterials* **2016**, *104*, 201–212.

[28] Panzella, L.; Gentile, G.; D'Errico, G.; Della Vecchia, N. F.; Errico, M. E.; Napolitano, A.; Carfagna, C.; d'Ischia, M. Atypical structural and π-electron features of a melanin polymer that lead to superior free-radical-scavenging properties. *Angew. Chem., Int. Ed.* **2013**, *52*, 12684–12687.

[29] Liu, Y.; Xiang, Y. P.; Zhen, Y. L.; Guo, R. Halide ion-induced switching of gold nanozyme activity based on Au-X interactions. *Langmuir* **2017**, *33*, 6372–6381.

[30] Bao, X. F.; Zhao, J. H.; Sun, J.; Hu, M.; Yang, X. R. Polydopamine nanoparticles as efficient scavengers for reactive oxygen species in periodontal disease. *ACS Nano* **2018**, *12*, 8882–8892.

[31] Lunov, O.; Syrovets, T.; Loos, C.; Nienhaus, G. U.; Mailänder, V.; Landfester, K.; Rouis, M.; Simmet, T. Amino-functionalized polystyrene nanoparticles activate the NLRP3 inflammasome in human macrophages. *ACS Nano* **2011**, *5*, 9648–9657.

[32] Li, F.; Li, T. Y.; Sun, C. X.; Xia, J. H.; Jiao, Y.; Xu, H. P. Selenium-doped carbon quantum dots for free-radical scavenging. *Angew. Chem., Int. Ed.* **2017**, *56*, 9910–9914.

[33] Sun, H. J.; Zhou, Y.; Ren, J. S.; Qu, X. G. Carbon nanozymes: Enzymatic properties, catalytic mechanism, and applications. *Angew. Chem., Int. Ed.* **2018**, *57*, 9224–9237.

[34] Huang, Y. Y.; Ren, J. S.; Qu, X. G. Nanozymes: Classification, catalytic mechanisms, activity regulation, and applications. *Chem. Rev.* **2019**, *119*, 4357–4412.

[35] Zhang, J. Y.; Wu, S. H.; Ma, L. Z.; Wu, P.; Liu, J. W. Graphene oxide as a photocatalytic nuclease mimicking nanozyme for DNA cleavage. *Nano Res.* **2020**, *13*, 455–460.

[36] Vernekar, A. A.; Sinha, D.; Srivastava, S.; Paramasivam, P. U.; D'Silva, P.; Mugesh, G. An antioxidant nanozyme that uncovers the cytoprotective potential of vanadia nanowires. *Nat. Commun.* **2014**, *5*, 5301.

[37] Zhang, W.; Hu, S. L.; Yin, J. J.; He, W. W.; Lu, W.; Ma, M.; Gu, N.; Zhang, Y. Prussian blue nanoparticles as multienzyme mimetics and reactive oxygen species scavengers. *J. Am. Chem. Soc.* **2016**, *138*, 5860–5865.

[38] Lin, S. C.; Cheng, Y.; Zhang, H.; Wang, X. Y.; Zhang, Y. Y.; Zhang, Y. J.; Miao, L. Y.; Zhao, X. Z.; Wei, H. Copper tannic acid coordination nanosheet: A potent nanozyme for scavenging ROS from cigarette smoke. *Small* **2020**, *15*, 1902123.

[39] Li, W.; Liu, Z.; Liu, C. Q.; Guan, Y. J.; Ren, J. S.; Qu, X. G. Manganese dioxide nanozymes as responsive cytoprotective shells for individual living cell encapsulation. *Angew. Chem., Int. Ed.* **2017**, *56*, 13661–13665.

[40] Yao, J.; Cheng, Y.; Zhou, M.; Zhao, S.; Lin, S. C.; Wang, X. Y.; Wu, J. J. X.; Li, S. R.; Wei, H. ROS scavenging Mn₃O₄ nanozymes for *in vivo* anti-inflammation. *Chem. Sci.* **2018**, *9*, 2927–2933.

[41] Xin, Q.; Jia, X. R.; Nawaz, A.; Xie, W. J.; Li, L. T.; Gong, J. R. Mimicking peroxidase active site microenvironment by functionalized graphene quantum dots. *Nano Res.* **2020**, *13*, 1427–1433.

[42] Lian, M. L.; Xue, Z. J.; Qiao, X. Z.; Liu, C.; Zhang, S.; Li, X.; Huang, C. H.; Song, Q.; Yang, W. S.; Chen, X. et al. Movable hollow nanoparticles as reactive oxygen scavengers. *Chem* **2019**, *5*, 2378–2387.

[43] Huang, Y. Y.; Liu, Z.; Liu, C. Q.; Ju, E. G.; Zhang, Y.; Ren, J. S.; Qu, X. G. Self-assembly of multi-nanozymes to mimic an intracellular antioxidant defense system. *Angew. Chem., Int. Ed.* **2016**, *55*, 6646–6650.

[44] Wang, H.; Wan, K. W.; Shi, X. H. Recent advances in nanozyme research. *Adv. Mater.* **2019**, *31*, 1805368.

[45] Huang, L.; Chen, J. X.; Gan, L. F.; Wang, J.; Dong, S. J. Single-atom nanozymes. *Sci. Adv.* **2019**, *5*, eaav5490.

[46] Ai, Y. J.; Hu, Z. N.; Liu, L.; Zhou, J. J.; Long, Y.; Li, J. F.; Ding, M. Y.; Sun, H. B.; Liang, Q. L. Magnetically hollow Pt nanocages with ultrathin walls as a highly integrated nanoreactor for catalytic transfer hydrogenation reaction. *Adv. Sci.* **2019**, *6*, 1802132.

[47] Yang, S. W.; Sun, J.; He, P.; Deng, X. X.; Wang, Z. Y.; Hu, C. Y.; Ding, G. Q.; Xie, X. M. Selenium doped graphene quantum dots as an ultrasensitive redox fluorescent switch. *Chem. Mater.* **2015**, *27*, 2004–2011.

[48] Zhu, S.; Zhou, H.; Hibino, M.; Honma, I.; Ichihara, M. Synthesis of MnO_2 nanoparticles confined in ordered mesoporous carbon using a sonochemical method. *Adv. Funct. Mater.* **2005**, *15*, 381–386.

[49] Zhu, W. W.; Dong, Z. L.; Fu, T. T.; Liu, J. J.; Chen, Q.; Li, Y. G.; Zhu, R.; Xu, L. G.; Liu, Z. Modulation of hypoxia in solid tumor microenvironment with MnO_2 nanoparticles to enhance photo-dynamic therapy. *Adv. Funct. Mater.* **2016**, *26*, 5490–5498.

[50] Chen, Q.; Feng, L. Z.; Liu, J. J.; Zhu, W. W.; Dong, Z. L.; Wu, Y. F.; Liu, Z. Intelligent albumin-MnO_2 nanoparticles as pH-/H_2O_2-responsive dissociable nanocarriers to modulate tumor hypoxia for effective combination therapy. *Adv. Mater.* **2016**, *28*, 7129–7136.